Enhancing risk prediction capabilities in patients with carotid artery disease using a 2-level computational approach

Panagiotis K. Siogkas, Dimitrios S. Pleouras, Vasilis D. Tsakanikas, Michalis D. Mantzaris, Vassiliki T. Potsika, Antonis Sakellarios, George Charalampopoulos, George Galyfos, Fragiska Sigala, and Dimitrios I. Fotiadis, *Fellow, IEEE*

***Abstract*— One of the main causes of death worldwide is carotid artery disease, which causes increasing arterial stenosis and may induce a stroke. To address this problem, the scientific community aims to improve our understanding of the underlying atherosclerotic mechanisms, as well as to make it possible to forecast the progression of atherosclerosis. Additionally, over the past several years, developments in the field of cardiovascular modeling have made it possible to create precise three-dimensional models of patient-specific main carotid arteries. The aforementioned 3D models are then implemented by computational models to forecast either the progression of atherosclerotic plaque or several flow-related metrics which are correlated to risk evaluation. A precise representation of both the blood flow and the fundamental atherosclerotic process within the arterial wall is made possible by computational models, therefore, allowing for the prediction of future lumen stenoses, plaque areas and risk prediction. This work presents an attempt to integrate the outcomes of a novel plaque growth model with advanced blood flow dynamics where the deformed luminal shape derived from the plaque growth model is compared to the actual patient-specific luminal model in terms of several hemodynamic metrics, to identify the prediction accuracy of the aforementioned model. Pressure drop ratios had a mean difference of <3%, whereas OSI-derived metrics were identical in 2/3 cases.**

***Clinical Relevance*—This establishes the accuracy of our plaque growth model in predicting the arterial geometry after the desired timeline.**

I. Introduction

According to a representative plaque growth model [1], the endothelium membrane is subjected to flow-induced shear stress, which affects the atherosclerotic process. More precisely, the endothelial function is altered in regions of low shear stresses, increasing endothelial permeability and causing an aberrant buildup of low-density lipoproteins (LDL) within the arterial wall. The infiltrating LDL is oxidized by the arterial wall's free radicals, which causes the generation of cytokines starting, therefore, an inflammatory response. The fundamental cells of the immune system, monocytes and T-cells, are drawn to the inflammatory mediators (cytokines) in order to take up the oxidized LDL, which results in the development of foam cells. Specifically, monocytes differentiate into macrophages, while T-cells activate the macrophages to uptake the oxidized LDL. Fatty streaks primarily consist of foam cells. Additionally, the cytokines that T-cells secrete cause contractile smooth muscle cells (SMCs) to proliferate and differentiate into synthetic smooth muscle cells that secrete collagen to heal the inflamed region. Foam cells, synthetic smooth muscle cells, and collagen are a few of the fundamental plaque species that are replicated, increasing the wall thickness while decreasing the lumen area [2]. Several models have been published over the past 20 years in an effort to forecast the growth of atherosclerotic plaque. Although only a few proof-of-concept investigations were based on actual human artery geometries [1-8], the majority of these studies used idealized 1D or 2D arterial geometries [9].

In this work, we compare the luminal geometry of patient-specific carotid arteries, as simulated with our in-house developed plaque growth computational model after 1 year, against the actual patient-specific arterial geometry as reconstructed, 1 year after the baseline MRI screening, in terms of hemodynamic parameters.

II. Materials & Methods

A. Dataset

Three patients with >50% carotid stenosis using a 1.5-T whole-body system (Signa HDx, GE Healthcare, Waukesha, WI, USA) with a bilateral four-channel phased-array carotid coil (Machnet BV, Eelde, the Netherlands) from the TAXINOMISIS cohort were used in the current study. Patient provided written informed consent and enrolled in the TAXINOMISIS clinical study (www.clinicaltrials.gov; ID: NCT03495830) protocol which was approved by the local competent ethics committee.

B. 3D reconstruction

The MRI images including the ToF, T1w, T2w and PD series were utilized by our in-house developed 3D reconstruction algorithm [10] to reconstruct the three Baseline cases, as well as the respective 1-year follow-up cases. The baseline 3D models were used by our plaque growth model, which is described below, and the simulated deformed 3D models were

*This work has received funding from the European Union's Horizon 2020 research and innovation programme under grant agreement No 755320, as part of the TAXINOMISIS project.

P. K. Siogkas, D. S. Pleouras, V. D. Tsakanikas, M. D. Mantzaris, V. T. Potsika and A. Sakellarios are with the Unit of Medical Technology and Intelligent Information Systems, Dept. of Materials Science and Engineering University of Ioannina, Ioannina, Greece (e-mail: psiogkas4454@gmail.com,dipleouras@gmail.com,vasilistsakanikas@gmail.com,dmantzaris@gmail.com,potsika@gmail.com, ansakel13@gmail.com).

F. Sigala, George Charalampopoulos and George Galyfos are with the First Propaedeutic Dept. of Surgery, National and Kapodistrian University of Athens, Hippocration Hospital, Athens, Greece (e-mail: drfsigala@yahoo.gr, charalampopoulosg@gmail.com, georgegalyfos@hotmail.com).

D. I. Fotiadis is with the Unit of Medical Technology and Intelligent Information Systems, Dept. of Materials Science and Engineering, University of Ioannina, and with the Biomedical Research Institute FORTH, University Campus of Ioannina, 45110 Ioannina, Greece (phone: +30 26510 09006; email: fotiadis@uoi.gr).

used for the comparison to the actual follow-up 3D models that were also reconstructed for the purposes of this work (Fig.1).

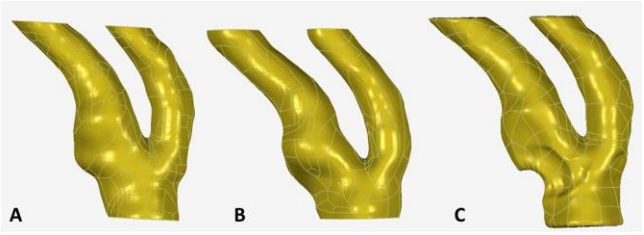

Fig. 1: A) Baseline actual lumen model, B) 1 year follow-up actual lumen model, and C) 1 year plaque growth simulated lumen model.

C. Plaque Growth Simulation

The simulation of plaque growth was accomplished by employing numerous differential equations to mimic the main biological processes of atherosclerosis, which is done in a 4-step modeling technique, as previously reported in detail.

1) Steady blood flow

Initially, a steady state simulation of the luminal blood flow is performed using the Navier-Stokes equations considering a laminar, incompressible and Newtonian flow [2, 4].

$$\frac{\partial}{\partial x_i}\left(\rho U_i U_j\right) = -\frac{\partial P}{\partial x_j} - \frac{\partial \tau_{ij}}{\partial x_i}, \tag{1}$$

$$\tau_{ij} = -\mu\left(\frac{\partial U_j}{\partial x_i} + \frac{\partial U_i}{\partial x_j} + \frac{2}{3}\delta_{ij}\mu\frac{\partial U_k}{\partial x_k}\right), \tag{2}$$

$$\frac{D\rho}{Dt} + \frac{\partial(\rho\,\mathbf{K}\cdot\mathbf{U})_i}{\partial x_i} = 0, \tag{3}$$

where, ρ is the blood density, U is the blood velocity, P is the pressure, τ is the shear stress, μ is the dynamic viscosity.

2) Flow-induced deformation of the arterial wall.

The flow-induced strain on the artery wall is taken into account in our study' second stage. An equation for linear stress and strain is used to calculate the strain distribution along the artery wall.

$$\boldsymbol{\sigma} = D\boldsymbol{\varepsilon}, \tag{4}$$

where, σ is the tensor of the structural stress, D is the arterial wall's elasticity modulus and ε is the tensor of the structural stress.

3) Atherosclerotic process

Modeling of the primary plaque formation mechanisms is done in the third phase [5], [14]. The transmural flow of plasma in the artery wall, which is represented by the modified Navier-Stokes equations that take the arterial wall's porosity into account, affects the species transfer.

$$\rho\gamma\frac{\partial U_j}{\partial t} + \frac{\partial}{\partial x_i}\left(\rho(\mathbf{K}\cdot\mathbf{U})_i U_j\right) = -\gamma\frac{\partial P}{\partial x_j} - \frac{\partial \tau_{ij}}{\partial x_i} + \gamma S_M, \tag{5}$$

$$\tau_{ij} = -\mu_{plasma}\left(\frac{\partial U_j}{\partial x_i} + \frac{\partial U_i}{\partial x_j} + \frac{2}{3}\delta_{ij}\mu\frac{\partial U_k}{\partial x_k}\right), \tag{6}$$

$$\frac{D\rho}{Dt} + \frac{\partial(\rho\,\mathbf{K}\cdot\mathbf{U})_i}{\partial x_i} = 0, \tag{7}$$

$$K^{ij} = \gamma\delta^{ij}, \tag{8}$$

where, γ is the volume porosity of the arterial wall and $\mathbf{K}$ is the area porosity tensor, which is a symmetric second rank tensor. According to Darcy's law, the momentum losses SM result from the permeability reduction:

$$S_{M,i} = -\frac{\mu_{plasma}}{K_{perm}}\mathbf{U}_i, \tag{9}$$

where, μ_{plasma} is the plasma viscosity, while K_{perm} is the Darcian permeability.

All of the species concentrations taken into consideration in the wall's domain are described by the modified convection-diffusion-reaction taking the effects of porosity into account:

$$\gamma\frac{\partial c}{\partial t} + \frac{\partial}{\partial x_i}\left((\boldsymbol{K}\cdot\boldsymbol{U})_j c\right) = D\frac{\partial}{\partial x_i}\left(\boldsymbol{K}\cdot\frac{\partial}{\partial x_j}c\right) + Sc, \tag{10}$$

where, c is the substance's concentration and D is the diffusivity.

The Kedem-Katchalsky equations, which assess the fluxes through bio-membranes based on the pressure and concentration variations across them [4, 11], characterize the endothelial fluxes. The endothelial monocyte and T-cell fluxes, however, are represented by experimental equations [4, 11], despite the fact that the LDL and HDL fluxes are well described by the Kedem-Katchalsky equations. The concentration of nitric oxide in the endothelium, which is also described by experimental equations [2, 4] and [12], affects the diffusive permeabilities of the LDL and HDL.

4) Arterial wall thickening & lumen narrowing

Arterial wall thickening and lumen narrowing are assessed using a linear stress-strain equation in the last stage (as Eq. 4). We assess the volumetric strain distribution of the artery wall, which is applied as a global condition to the model, using the simulated species concentrations. The boundary condition for the adventitia and the arterial wall side regions is frictionless support. This method simulates the inward remodeling of the vascular wall to permit wall thickening (wall thickening).

D. 1 year follow-up blood flow modeling

The 3D reconstructed pairs of luminal carotid geometries were then subjected to transient blood flow simulations, using the exact same patient and time-specific boundary conditions, as extracted from carotid UltraSound (US) screening. At the inlet, a patient-specific mass flow rate for an entire cardiac cycle was used as a boundary condition. The same applies for the external carotid artery (ECA), where a patient-specific mass flow rate profile is calculated and applied as an outlet boundary condition. The cardiac cycle duration is calculated from the patient-specific measured beats per minute and timesteps of 0.05 seconds are used to divide the cardiac cycle.

Regarding the internal carotid artery (ICA), a zero-pressure boundary condition is applied as an outlet. A no-slip and no penetration boundary condition is applied at the arterial wall. In order to calculate the pressure drop ratios between the CCA and the ICA or ECA outlets, the following procedure is followed: using a zero-pressure boundary condition for the ICA outlet, we calculate the pressure gradient throughout the entire vessel. Having the patient-specific mean arterial pressure value for the CCA which is calculated using Eq.11, we calculate the pressure difference for the simulated case between the CCA and the ECA and we subtract it from the patient-specific value, thus calculating the actual pressure for the ICA outlet.

$$MAP = \frac{SBP + 2(DBP)}{3}, \tag{11}$$

where MAP is the Mean Arterial Pressure, SBP the Systolic Blood Pressure and DBP the Diastolic Blood Pressure, respectively. The same process is then followed between the CCA and the ECA and the final ECA outlet pressure value is calculated, thus allowing for the calculation of the two pressure drop ratios, respectively (i.e., P_{ECA}/P_{CCA} and P_{ICA}/P_{CCA}). In order to model blood flow in our simulations, we used the Navier-Stokes (Eq. 1-3) and the continuity equations (Eq. 13):

$$\nabla \bullet (\rho \mathbf{v}) = 0, \tag{13}$$

Blood was treated as Newtonian with density 1050 kg/m^3 and dynamic viscosity 0.0035 Pa·s, respectively. All simulations were carried out using ANSYS® v16.2. The element size was set to 0.16 mm or lower and constituted only of tetrahedra. The convergence criterion was set to 10^{-4} and the iteration limit was 150 for each timestep. Time-averaged endothelial shear stress (TAESS) values, total area of low ESS (i.e., <2 Pa), oscillatory shear index (OSI) values, normalized TAESS, normalized OSI values, and P_{ECA}/P_{CCA} and P_{ICA}/P_{CCA} ratios were calculated for each arterial pair. OSI is calculated as:

$$OSI = \frac{1}{2}\left(1 - \frac{\int_0^T ESSdt}{\int_0^T ESSdt}\right). \tag{16}$$

where T is the cardiac cycle period used to calculate the time-averaged endothelial shear stress, and ESS is the endothelial shear stress.

III. RESULTS

The analysis was based on a series of important hemodynamic metrics that were calculated by the previously described blood flow simulations. All calculations were made on the three pairs of 3D luminal geometries, regarding the three examined cases. Table 1 depicts the calculated metrics values for all simulated cases. Briefly, the peak TAESS values exhibited a modestly close match, the pressure drop ratios were almost identical, the average TAESS exhibited very similar values for the three pairs of vessels and the average vessel OSI values were also almost identical. Finally, the very important normalized areas of low TAESS and high OSI were significantly correlated between them. Figures 2-4 depict the calculated areas of low TAESS and high OSI values for all three cases, respectively.

Table 1: Calculated blood flow metrics for all 3 pairs of cases

Artery	peak TAWSS (Pa)	P_{ICA}/P_{CCA}	P_{ECA}/P_{CCA}	Vessel average TAWSS (Pa)	Vessel average OSI	Area of low TAWSS/Total vessel area (%)	Area of high OSI/Total vessel area (%)
22-Deformed	60.14	0.98	0.93	15.1	0.12	4.98	11.6
22-Actual	68.9	0.96	0.91	16.6	0.1	6.31	11.8
14-Deformed	35.2	0.97	0.99	10.2	0.14	9.81	11.7
14-Actual	38.3	0.98	0.99	9.1	0.12	9.30	8.4
11-Deformed	65.3	0.93	1.00	8.8	0.18	21.28	20.3
11-Actual	58.9	0.96	1.00	7.69	0.18	24.77	20.5

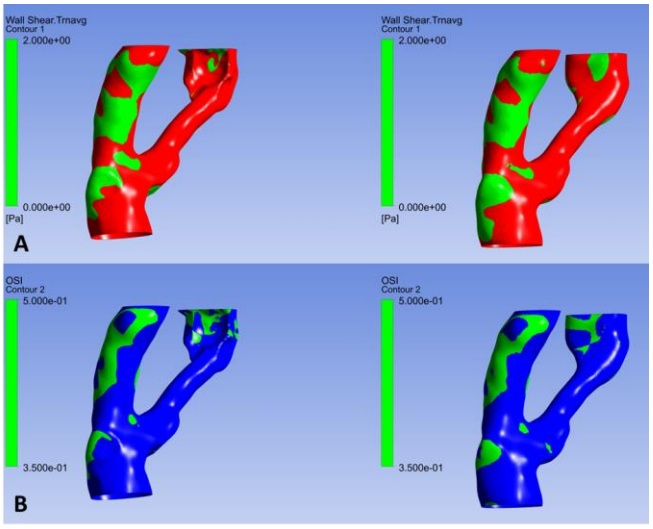

Fig. 2: Case 22_Lumen-A) Areas of low TAESS are depicted in green. B) Areas of high OSI values are depicted in green.

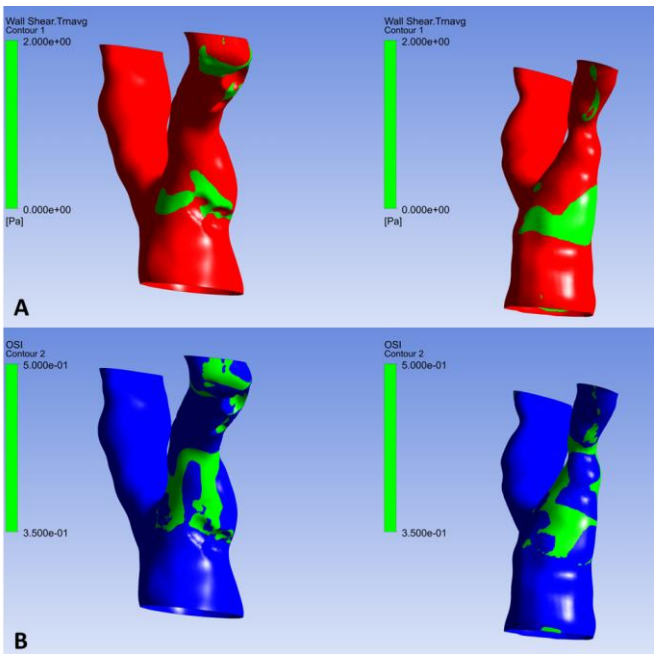

Fig. 3: Case 14_Lumen-A) Areas of low TAESS are depicted in green. B) Areas of high OSI values are depicted in green.

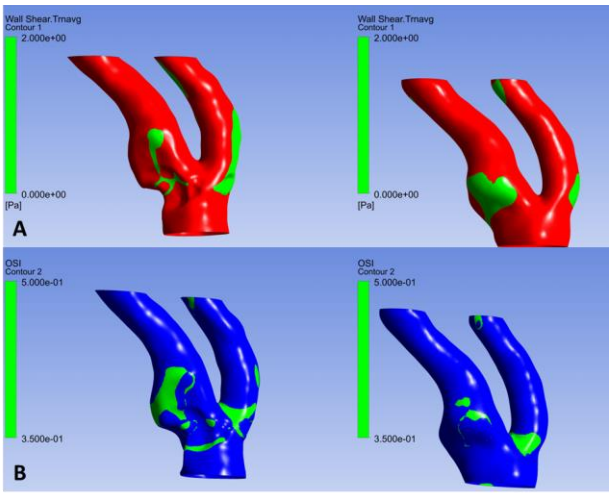

Fig. 4: Case 11_Lumen-A) Areas of low TAESS are depicted in green. B) Areas of high OSI values are depicted in green.

IV. DISCUSSION

In this proof-of-concept study, we presented the geometrical outcomes of our plaque growth computational models which were compared to the respective patient-specific follow-up 3D luminal models in terms of hemodynamic response, using a series of important metrics. Patient-specific boundary conditions during the 1st year follow-up were used for each case (i.e., both in the simulated deformed model and the actual follow-up 3D model) to avoid any miscalculations caused by different boundary conditions. Furthermore, the exact same mesh strategy was used for all pairs. The calculated results were very promising, both numerically and topologically. The vessel average TAESS values exhibited comparable values, with a mean deviation of ~10%, whereas the peak TAESS values exhibited a mean difference of ~9.8%. The differences that were observed regarding the pressure drop ratios were evidently smaller, and regarding case 14, we had almost identical values, whereas for the remaining two cases, the mean difference didn't exceed 2%. Regarding areas of high OSI (i.e., OSI>0.35), they are generally considered as prone to present with endothelial dysfunction and plaque development [13]. The normalized areas of high OSI values were almost identical for the two cases, and only in one case did they exhibit a significant mismatch. Regarding the areas of low TAESS (i.e. TAESS<2 Pa), they are known to be prone for plaque development or progression [14]. The values of the normalized areas of low TAESS were also highly comparable between them. The main limitation of our study is the relatively small number of examined cases, however, it is evident that the plaque growth model that we have established is capable of producing promising results regarding the evolution of the arterial geometries within time. Furthermore, the differences observed in the peak TAESS values can be partially explained by the fact that the model produces 3D formations regarding the plaque components that may include crease angles, thus explaining the ESS differences with the actual 3D geometries of the follow-up time point.

V. CONCLUSION

In this work we presented a comparison between the 3D arterial luminal geometries produced by our in-house developed plaque growth model after one year, and the actual 1-year follow-up models reconstructed using our in-house developed reconstruction algorithm. The vessel-specific computational results indicated a promising correlation between the three pairs of geometries in hemodynamic terms, thus exhibiting the efficiency of our plaque growth model.

REFERENCES

[1] D. Pleouras *et al.*, "Atherosclerotic Plaque Growth Prediction in Coronary Arteries using a Computational Multi-level Model: The Effect of Diabetes," in *2019 IEEE 19th International Conference on Bioinformatics and Bioengineering (BIBE)*, 28-30 Oct. 2019 2019, pp. 702-705, doi: 10.1109/BIBE.2019.00132.

[2] D. S. Pleouras *et al.*, "Simulation of atherosclerotic plaque growth using computational biomechanics and patient-specific data," *Sci Rep*, vol. 10, no. 1, p. 17409, Oct 15 2020, doi: 10.1038/s41598-020-74583-y.

[3] A. Sakellarios *et al.*, "Prediction of atherosclerotic disease progression using LDL transport modelling: a serial computed tomographic coronary angiographic study," *Eur Heart J Cardiovasc Imaging*, vol. 18, no. 1, pp. 11-18, Jan 2017, doi: 10.1093/ehjci/jew035.

[4] A. I. Sakellarios *et al.*, "Prediction of Atherosclerotic Plaque Development in an In Vivo Coronary Arterial Segment Based on a Multilevel Modeling Approach," *IEEE Trans Biomed Eng*, vol. 64, no. 8, pp. 1721-1730, Aug 2017, doi: 10.1109/TBME.2016.2619489.

[5] D. Pleouras *et al.*, "A computational multi-level atherosclerotic plaque growth model for coronary arteries," *Annu Int Conf IEEE Eng Med Biol Soc*, vol. 2019, pp. 5010-5013, Jul 2019, doi: 10.1109/EMBC.2019.8857329.

[6] P. Siogkas *et al.*, "Multiscale-patient-specific artery and atherogenesis models," *IEEE Trans Biomed Eng*, vol. 58, no. 12, pp. 3464-8, Dec 2011, doi: 10.1109/TBME.2011.2164919.

[7] M. D. Mantzaris *et al.*, "Computational modeling of atherosclerotic plaque progression in carotid lesions with moderate degree of stenosis()," *Annu Int Conf IEEE Eng Med Biol Soc*, vol. 2021, pp. 4209-4212, Nov 2021, doi: 10.1109/EMBC46164.2021.9630376.

[8] D. S. Pleouras *et al.*, "Prediction of the atherosclerotic plaque development in carotid arteries; the effect of T-cells," *Annu Int Conf IEEE Eng Med Biol Soc*, vol. 2022, pp. 1590-1593, Jul 2022, doi: 10.1109/EMBC48229.2022.9871632.

[9] M. Guo, Y. Cai, X. Yao, and Z. Li, "Mathematical modeling of atherosclerotic plaque destabilization: Role of neovascularization and intraplaque hemorrhage," *J Theor Biol*, vol. 450, pp. 53-65, Aug 7 2018, doi: 10.1016/j.jtbi.2018.04.031.

[10] V. D. Tsakanikas *et al.*, "A deep learning oriented method for automated 3D reconstruction of carotid arterial trees from MR imaging," *Annu Int Conf IEEE Eng Med Biol Soc*, vol. 2020, pp. 2408-2411, Jul 2020, doi: 10.1109/EMBC44109.2020.9176532.

[11] M. Cilla, E. Pena, and M. A. Martinez, "Mathematical modelling of atheroma plaque formation and development in coronary arteries," *J R Soc Interface*, vol. 11, no. 90, p. 20130866, Jan 6 2014, doi: 10.1098/rsif.2013.0866.

[12] M. A. Bulelzai and J. L. Dubbeldam, "Long time evolution of atherosclerotic plaques," *J Theor Biol*, vol. 297, pp. 1-10, Mar 21 2012, doi: 10.1016/j.jtbi.2011.11.023.

[13] D. N. Ku, D. P. Giddens, C. K. Zarins, and S. Glagov, "Pulsatile flow and atherosclerosis in the human carotid bifurcation. Positive correlation between plaque location and low oscillating shear stress," *Arteriosclerosis*, vol. 5, no. 3, pp. 293-302, May-Jun 1985, doi: 10.1161/01.atv.5.3.293.

[14] N. Sun, R. Torii, N. B. Wood, A. D. Hughes, S. A. Thom, and X. Y. Xu, "Computational modeling of LDL and albumin transport in an in vivo CT image-based human right coronary artery," *J Biomech Eng*, vol. 131, no. 2, p. 021003, Feb 2009, doi: 10.1115/1.3005161.